symmetry

MDPI

Article

Quantifying the Nonadiabaticity Strength Constant in Recently Discovered Highly Compressed Superconductors

Evgeny F. Talantsev [1,2]

[1] M. N. Miheev Institute of Metal Physics, Ural Branch, Russian Academy of Sciences, 18, S. Kovalevskoy St., 620108 Ekaterinburg, Russia; evgeny.talantsev@imp.uran.ru; Tel.: +7-912-676-0374

[2] NANOTECH Centre, Ural Federal University, 19 Mira St., 620002 Ekaterinburg, Russia

Abstract: Superconductivity in highly pressurized hydrides has become the primary direction for the exploration of the fundamental upper limit of the superconducting transition temperature, T_c, after Drozdov et al. (*Nature* **2015**, *525*, 73) discovered a superconducting state with $T_c = 203\ K$ in highly compressed sulfur hydride. To date, several dozen high-temperature superconducting polyhydrides have been discovered and, in addition, it was recently reported that highly compressed titanium and scandium exhibit record-high T_c (up to 36 K). This exceeded the $T_c = 9.2\ K$ value of niobium many times over, which was the record-high T_c ambient pressure metallic superconductor. Here, we analyzed the experimental data for the recently discovered high-pressure superconductors (which exhibit high transition temperatures within their classes): elemental titanium (Zhang et al., *Nature Communications* **2022**; Liu et al., *Phys. Rev. B* **2022**), TaH_3 (He et al., *Chinese Phys. Lett.* **2023**), $LaBeH_8$ (Song et al., *Phys. Rev. Lett.* **2023**), black phosphorous (Li et al., *Proc. Natl. Acad. Sci.* **2018**; Jin et al., *arXiv* **2023**), and violet (Wu et al., *arXiv* **2023**) phosphorous to reveal the nonadiabaticity strength constant $\frac{T_\theta}{T_F}$ (where T_θ is the Debye temperature, and T_F the Fermi temperature) in these superconductors. The analysis showed that the δ-phase of titanium and black phosphorous exhibits $\frac{T_\theta}{T_F}$ scores that are nearly identical to those associated with A15 superconductors, while the studied hydrides and violet phosphorous exhibit constants in the same ballpark as those of H_3S and LaH_{10}.

Keywords: hydrogen-rich superconductors; highly compressed superconductors; electron–phonon coupling constant; Debye temperature; nonadiabaticity

Citation: Talantsev, E.F. Quantifying the Nonadiabaticity Strength Constant in Recently Discovered Highly Compressed Superconductors. *Symmetry* **2023**, *15*, 1632. https://doi.org/10.3390/sym15091632

Academic Editors: Hongzhi Shen and Yehong Chen

Received: 12 July 2023
Revised: 31 July 2023
Accepted: 4 August 2023
Published: 24 August 2023

1. Introduction

The discovery of near-room-temperature superconductivity in highly compressed sulfur hydride by Drozdov et al. [1] presented a new era in superconductivity. This research field represents one of the most fascinating scientific and technological explorations in modern condensed-matter physics. In this area of research, advanced first-principles calculations [2–11] are essential parts of the experimental quest for the discovery of new hydrides phases [12–21], and both of these directions drive the development of new experimental techniques with which to study highly pressurized materials [22–31].

From 2015 until now, several dozen high-temperature superconducting polyhydride phases have been discovered and studied [1,12–21,24,32–45]. At the same time, high-pressure studies of superconductivity and high-pressure material synthesis [46–48] in non-hydrides (including cuprates [49–52]) have also progressed [53–62], including the observation of $T_c > 26\ K$ in highly compressed elemental titanium [63,64] and scandium [65,66], and the discovery that $T_c^{onset} \cong 78\ K$ [67,68] and $T_c^{zero} \cong 45\ K$ [69] in $La_3Ni_2O_7$.

First-principles calculations [12–21,70–79] are essential tools in the quest for room-temperature superconductivity (they were used [76] to explain the experimental results [80] for one of the most difficult-to-explain hydride cases, AlH_3), and the primary calculated parameter in these calculations is the transition temperature, T_c. In addition, another difficult-to-explain hydride should be mentioned, which is $LiPdH_x$ [46]. This hydride was synthesized at high pressure in a bulk form [46]; however, as was predicted by the first-principles calculations, the high transition temperature [81] was not confirmed by the experiment [46].

Thus, the experiment [1,3,25] remains the final criterion. Therefore, the confirmation of the predicted T_c in order to determine the other fundamental ground-state parameters, including the upper critical field, $B_{c2}(0)$; the lower critical field, $B_{c1}(0)$ [12,22]; the self-field critical current density, $J_c(sf,T)$ [24,82–84]; the London penetration depth, $\lambda(0)$ [22,23,85,86]; the superconducting energy gap amplitude, $\Delta(0)$ [87–89]; and gap symmetry [90,91]; is the task of the experiment and the data analysis.

Another complication in understanding the superconductivity of highly-pressurized materials is the phenomenon of nonadiabaticity, which originates from the fact that the Migdal–Eliashberg theory of the electron–phonon-mediated superconductivity [92,93] is based on the primary assumption/postulate that the superconductor obeys the inequality:

$$T_\theta \ll T_F \tag{1}$$

where T_θ is the Debye temperature and T_F is the Fermi temperature. In other words, Equation (1) implies that the superconductor exhibits fast electric charge carriers and slow ions. This assumption simplifies the theoretical model of electron–phonon-mediated superconductivity; however, Equation (1) is not satisfied for many unconventional superconductors [94–102] (which was first pointed out by Pietronero and co-workers [103–106]) and many highly compressed superconductors [91,101,107–109].

While the theoretical aspects of the nonadiabatic effects can be found elsewhere [11,94,100,103–107], in practice, the strength of the nonadiabatic effects can be quantified via the $\frac{T_\theta}{T_F}$ ratio [101,102], for which, in Ref. [101], three characteristic ranges were proposed:

$$\begin{cases} \frac{T_\theta}{T_F} < 0.025 \rightarrow \textit{adiabatic superconductor}; \\ 0.025 \lesssim \frac{T_\theta}{T_F} \lesssim 0.4 \rightarrow \textit{moderately strong nonadiabatic superconductor}; \\ 0.4 < \frac{T_\theta}{T_F} \rightarrow \textit{nonadiabatic superconductor}. \end{cases} \tag{2}$$

It was found in Ref. [101], and confirmed in Ref. [91], that superconductors with $T_c > 10\ K$ (from a dataset of 46 superconductors from all major superconductor families) exhibit the $\frac{T_\theta}{T_F}$ ratio in the range $0.025 \lesssim \frac{T_\theta}{T_F} \lesssim 0.4$.

This is an interesting and theoretically unexplained empirical observation.

In this study, we further extended the empirical $\frac{T_\theta}{T_F}$ database by deriving several fundamental parameters:

(1) the Debye temperature, T_θ;
(2) the electron–phonon coupling constant, λ_{e-ph};
(3) the ground-state coherence length, $\xi(0)$;
(4) the Fermi temperature, T_F;
(5) the nonadiabaticity strength constant, $\frac{T_\theta}{T_F}$;
(6) and the ratio, $\frac{T_c}{T_F}$;

for five recently discovered highly compressed superconductors for which the reported raw experimental data are enough to deduce the above-mentioned parameters. These superconductors represent materials with high or record-high T_c in their families:

(1) elemental titanium, $\delta - Ti$ [63,64];
(2) TaH_3 [21];
(3) $LaBeH_8$ [110];
(4) black phosphorous [111–114];
(5) violet phosphorous [62].

In the result, we derived the nonadiabaticity strength constant, $\frac{T_\theta}{T_F}$, for these superconductors. Derived $\frac{T_\theta}{T_F}$ values confirmed the previously reported empirical observation [91,101] that the superconductors with $T_c > 10\ K$ obey the condition $0.025 \lesssim \frac{T_\theta}{T_F} \lesssim 0.4$.

2. Utilized Models and Data Analysis Tools

2.1. Debye Temperature

Within electron–phonon phenomenology, the Debye temperature, T_θ, is a fundamental parameters that determines the superconducting transition temperature, T_c [93,115–119]. T_θ can be deduced as a free-fitting parameter from a fit of temperature-dependent resistance, $R(T)$, to the Bloch–Grüneisen (BG) equation [120–123]:

$$R(T) = \frac{1}{\frac{1}{R_{sat}} + \frac{1}{R_0 + A\left(\frac{T}{T_\theta}\right)^5 \int_0^{\frac{T_\theta}{T}} \frac{x^5}{(e^x-1)(1-e^{-x})} dx}}, \tag{3}$$

where R_{sat}, R_0, T_θ, and A are free-fitting parameters.

2.2. The Electron–Phonon Coupling Constant

From the deduced T_θ, the electron–phonon coupling constant, λ_{e-ph}, can be calculated as the root of advanced McMillan equation [116–119]:

$$T_c = \left(\frac{1}{1.45}\right) \times T_\theta \times e^{-\left(\frac{1.04(1+\lambda_{e-ph})}{\lambda_{e-ph} - \mu^*(1+0.62\lambda_{e-ph})}\right)} \times f_1 \times f_2^*, \tag{4}$$

where

$$f_1 = \left(1 + \left(\frac{\lambda_{e-ph}}{2.46(1+3.8\mu^*)}\right)^{3/2}\right)^{1/3}, \tag{5}$$

$$f_2^* = 1 + (0.0241 - 0.0735 \times \mu^*) \times \lambda_{e-ph}^2, \tag{6}$$

where μ^* is the Coulomb pseudopotential parameter, which we assumed to be $\mu^* = 0.13$ (which is the typical value utilized in the first-principles calculation for many electron–phonon-mediated superconductors [63,124]). In Equations (4)–(6), we defined the T_c by a strict resistance criterion of $\frac{R(T)}{R_{norm}} \to 0$, where R_{norm} is the sample resistance at the onset of the transition.

2.3. Ground-State Coherence Length

We used a model proposed by Baumgartner et al. [125–127] to fit the upper critical field dataset, $B_{c2}(T)$, and determine the ground-state coherence length $\xi(0)$:

$$B_{c2}(T) = \frac{1}{0.693} \times \frac{\phi_0}{2\pi\xi^2(0)} \times \left(\left(1 - \frac{T}{T_c}\right) - 0.153 \times \left(1 - \frac{T}{T_c}\right)^2 - 0.152 \times \left(1 - \frac{T}{T_c}\right)^4\right), \tag{7}$$

where $\phi_0 = \frac{h}{2e}$ is the superconducting flux quantum, $h = 6.626 \times 10^{-34}\ J \cdot s$ is Planck constant, $e = 1.602 \times 10^{-19}$ C, and $\xi(0)$ and $T_c \equiv T_c(B=0)$ are free fitting parameters.

2.4. The Fermi Temperature

The Fermi temperature, T_F, can be calculated by using a simple expression of the free-electron model [128,129]:

$$T_F = \frac{\varepsilon_F}{k_B} = \frac{(3\pi^2 n \hbar^3)^{\frac{3}{2}}}{2m_e\left(1 + \lambda_{e-ph}\right)k_B} \tag{8}$$

where $m_e = 9.109 \times 10^{-31}\ kg$ is bare electron mass, $\hbar = 1.055 \times 10^{-34}\ J \cdot s$ is reduced Planck constant, $k_B = 1.381 \times 10^{-23}\ m^2 \cdot kg \cdot s^{-2} \cdot K^{-1}$ is Boltzmann constant, and n is the charge carrier density per volume (m^{-3}). Equation (8) can be used if the Hall resistance experiments are performed, and the charge carrier density, n, is established.

If Hall resistance measurements do not perform, then T_F can be calculated using the equation [58,59]:

$$T_F = \frac{\pi^2 m_e}{8 k_B} \times \left(1 + \lambda_{e-ph}\right) \times \xi^2(0) \times \left(\frac{\alpha k_B T_c}{\hbar}\right)^2 \quad (9)$$

where $\alpha = \frac{2\Delta(0)}{k_B \cdot T_c}$ is the gap-to-transition temperature ratio. This parameter is the only unknown parameter in Equation (9).

2.5. The Gap-to-Transition Temperature Ratio

To calculate the Fermi temperature using Equation (9), there is a need to know $\alpha = \frac{2\Delta(0)}{k_B \cdot T_c}$. To determine $\alpha = \frac{2\Delta(0)}{k_B \cdot T_c}$, we utilized the following approach. Carbotte [124] collected various parameters for 32 electron–phonon-mediated superconductors that exhibit $0.43 \leq \lambda_{e-ph} \leq 3.0$ and $3.53 \leq \frac{2\Delta(0)}{k_B \cdot T_c} \leq 5.19$. In Figure 1, we presented the dataset reported by Carbotte in Table IV [124]. The dependence $\frac{2\Delta(0)}{k_B \cdot T_c}$ vs.λ_{e-ph} can be approximated using a linear function (Figure 1) [130]:

$$\frac{2\Delta(0)}{k_B T_c} = C + D \times \lambda_{e-ph}, \quad (10)$$

where $C = 3.26 \pm 0.06$, and $D = 0.74 \pm 0.04$.

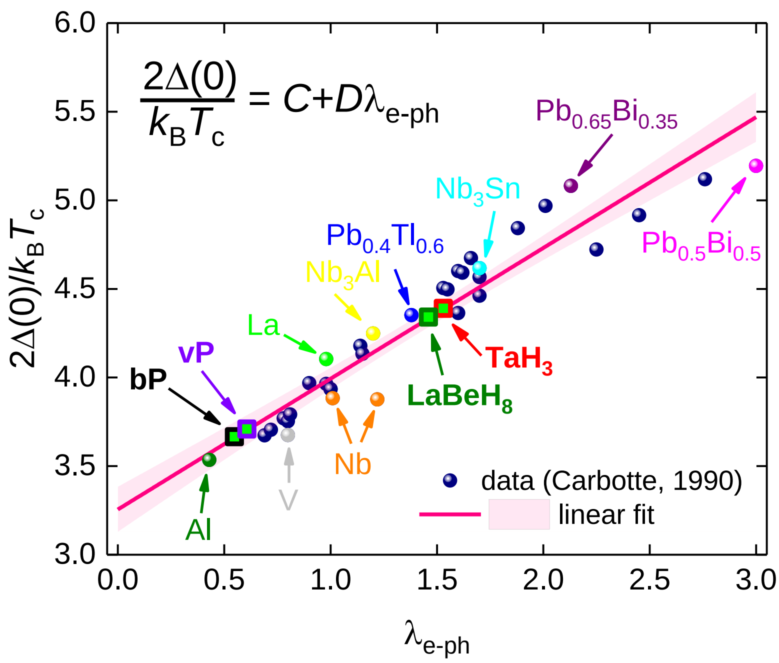

Figure 1. The gap-to-transition temperature ratio, $\frac{2 \cdot \Delta(0)}{k_B \cdot T_c}$, vs. the electron–phonon coupling constant, λ_{e-ph}, dataset reported by Carbotte in Table IV of Ref. [124]. A linear fit is shown by the pink line. Positions for some representative superconductors and superconductors studied in this report (where **bP** stands for black phosphorus and **vP** stands for violet phosphorus) are shown. The pink shadow area indicates 95% confidence bands for the linear fit.

Insofar as λ_{e-ph} is known, the $\frac{2\Delta(0)}{k_B \cdot T_c}$ ratio can be estimated from Equation (10).

3. Results

3.1. Highly Compressed Titanium

Zhang et al. [63] and Liu et al. [64] reported record-high T_c in the $\delta - Ti$ phase compressed at megabar pressures. In Figure 2, we show the fit of the $R(T)$ dataset measured by Zhang et al. [63] for the $\omega - Ti$ phase compressed at $P = 18GPa$ to Equation (3).

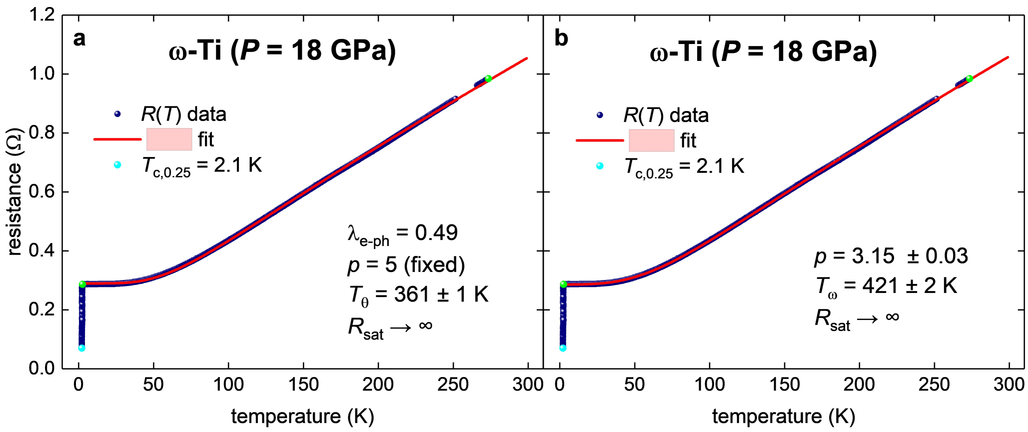

Figure 2. Temperature-dependent resistance data, $R(T)$, for compressed titanium ($\omega - Ti$-phase at P = 18 GPa) and data fit to Equation (3) (raw data reported by Zhang et al. [63]). Green balls indicate the bounds for which $R(T)$ data were used for the fit to Equation (3). (**a**) Fit to Debye model: $p = 5\ (fixed)$, $T_\theta = (361 \pm 1)\ K$, $T_{c,0.25} = 2.1\ K$, $\lambda_{e-ph} = 0.49$, fit quality is 0.99988. (**b**) Fit to Equation (3): $p = 3.15 \pm 0.03$, $T_\omega = (421 \pm 2)\ K$, $T_{c,0.25} = 2.1\ K$, fit quality is 0.99995. The pink shadow areas in both panels show 95% confidence bands.

The deduced Debye temperature (Figure 2a) for $\omega - Ti$-phase ($P = 18\ GPa$) is $T_\theta = 361 \pm 1\ K$. This value is within the ballpark value for $T_\theta(298\ K) = 380\ K$ for uncompressed titanium, which exhibits a $\alpha - Ti$ phase [131].

To calculate the electron–phonon coupling strength constant, λ_{e-ph}, using Equations (4)–(6), we defined the superconducting transition temperature, $T_c = 2.1\ K$, with the $\frac{R(T)}{R_{norm}} = 0.25$ criterion. This criterion was chosen based on the lowest temperature at which experimental $R(T)$ data measuring at $P = 18\ GPa$ were reported by Zhang et al. [63]. The deduced value $\lambda_{e-ph} = 0.49$ is very close to the $\lambda_{e-ph} = 0.43$ of pure elemental aluminum (Figure 1, and Ref. [124]).

We also confirmed the power-law exponent $n = 3.1$ (reported by Zhang et al. [63]) for the temperature-dependent $R(T)$. Zhang et al. [63] extracted this power-law exponent from the simple power-law fit of $R(T)$ at the temperature range of 3 $K \le T \le 70\ K$:

$$R(T) = R_0 + X \times T^n, \quad (11)$$

where R_0, X, and n are free-fitting parameters. As we showed earlier [132], Equation (11) does not always return correct n-values. The reliable approach is to fit the $R(T)$ data to Equation (3), where p is a free-fitting parameter. For the given case, our fit to Equation (3) (Figure 2b) returns the same power-law exponent, $p = 3.15 \pm 0.03$, as the one reported by Zhang et al. [63].

In Figure 3, we show $R(T)$ data measured by Zhang et al. [63] and Liu et al. [64] and the results of data fitting to Equations (3)–(7) for the $\delta - Ti$ phase compressed at $P = 154\ GPa$ (Figure 3a), $P = 180\ GPa$ (Figure 3b), $P = 183\ GPa$ (Figure 3c), and $P = 245\ GPa$ (Figure 3d).

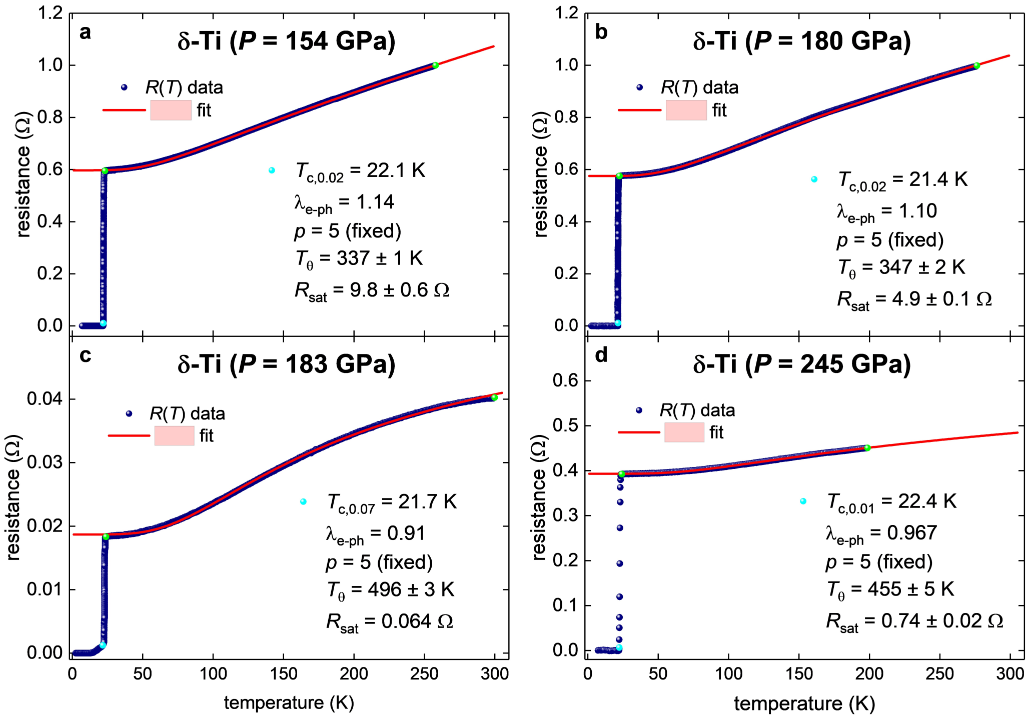

Figure 3. Temperature-dependent resistance data, $R(T)$, for compressed titanium ($\delta - Ti$-phase) and fit to the Debye model (Equation (3), $p = 5\ (fixed)$). Raw data were reported by Zhang et al. [63] (Panels (**a**,**b**,**d**)) and Liu et al. [64] (Panel (**c**)). Green balls indicate the bounds for which $R(T)$ data were used for the fit to Equation (3). Deduced parameters are (**a**) $T_\theta = (337 \pm 1)\ K$, $T_{c,0.02} = 22.1\ K$, $\lambda_{e-ph} = 1.14$, fit quality is 0.99992. (**b**) $T_\theta = (347 \pm 2)\ K$, $T_{c,0.02} = 21.4\ K$, $\lambda_{e-ph} = 1.10$, fit quality is 0.9998. (**c**) $T_\theta = (496 \pm 3)\ K$, $T_{c,0.07} = 21.7\ K$, $\lambda_{e-ph} = 0.91$, fit quality is 0.9996. (**d**) $T_\theta = (455 \pm 5)\ K$, $T_{c,0.01} = 22.4\ K$, $\lambda_{e-ph} = 0.967$, fit quality is 0.9997. The pink shadow areas show 95% confidence bands.

Liu et al. [64] reported λ_{e-ph} and logarithmic frequency ω_{log} for highly compressed titanium over a wide range of applied pressure calculated using first-principles calculations. In Figure 4, we present a comparison of the deduced λ_{e-ph} and T_θ values from the experiment and show the calculation results [64]. To compare ω_{log} (calculated using first-principles calculations) and T_θ deduced from the experiment, we used the theoretical expression proposed by Semenok [133]:

$$\frac{1}{0.827} \times \frac{\hbar}{k_B} \times \omega_{log} \cong T_\theta. \quad (12)$$

In Figure 4c, we also show T_F values calculated using Equation (8), where we used derived λ_{e-ph} and bulk density of charge carriers in compressed titanium, n, measured by Zhang et al. [63]. Zhang et al. [63] reported the $R(T)$ and n measured at different pressures. For T_F, calculations we assumed the following approximations: $n(P = 18\ GPa) = n(P = 31\ GPa) = 1.72 \times 10^{28}\ m^{-3}$; $n(P = 154\ GPa) = 2.39 \times 10^{28}\ m^{-3}$; and $n(P = 180\ GPa) = n(P = 183\ GPa) = n(P = 177\ GPa) = 1.70 \times 10^{28}\ m^{-3}$.

The evolution of the adiabaticity strength constant $\frac{T_\theta}{T_F}$ vs. pressure is shown in Figure 4c.

Figure 4 shows a very good agreement between values calculated using first-principles calculations and extracted from experiment λ_{e-ph} and characteristic phonon temperatures, T_θ and $\frac{1}{0.827} \times \frac{\hbar}{k_B} \times \omega_{log}$, at low and high applied pressures. More experimental data are required to perform detailed comparison.

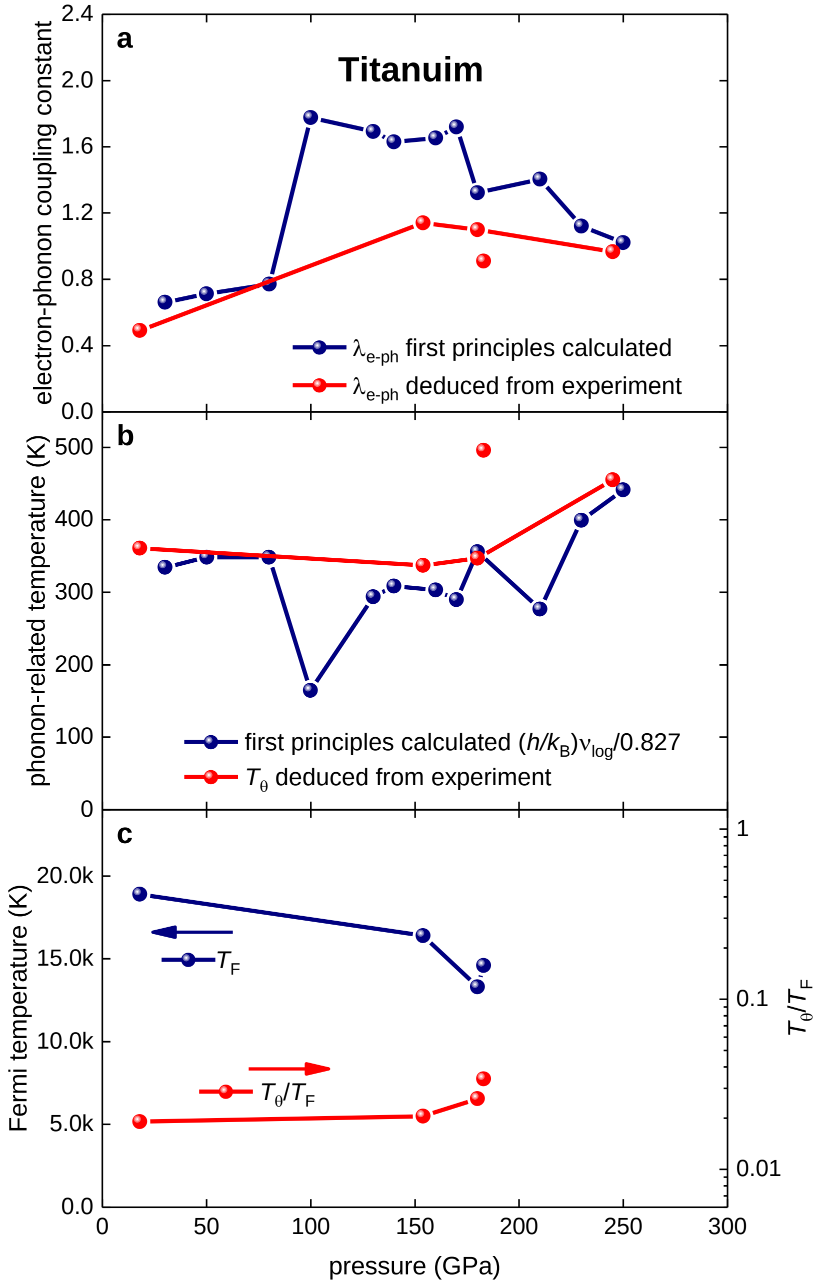

Figure 4. Evolution of (**a**) the electron–phonon coupling constant λ_{e-ph}; (**b**) characteristic phonon temperatures T_θ and $\frac{1}{0.827} \times \frac{\hbar}{k_B} \times \omega_{log}$; and (**c**) Fermi temperature, T_F, calculated using Equation (8) and the used of carrier density reported by Zhang et al. [63] and deduced λ_{e-ph} (in Panel (**a**)) and the nonadiabaticity strength constant, $\frac{T_\theta}{T_F}$, for highly compressed titanium.

The derived T_F, λ_{e-ph}, and $\frac{T_\theta}{T_F}$, values for highly compressed titanium are shown in Figures 5–7, together with values for the main superconducting families. It should be noted that other global scaling laws utilize different variables [83,134–140].

It is interesting to mention that $\delta - Ti$ is located close to A15 superconductors in all these plots (Figures 5–7). This proximity can be interpreted as a reflection that the highest performance of the electron–phonon-mediated superconductivity is achieved for these materials.

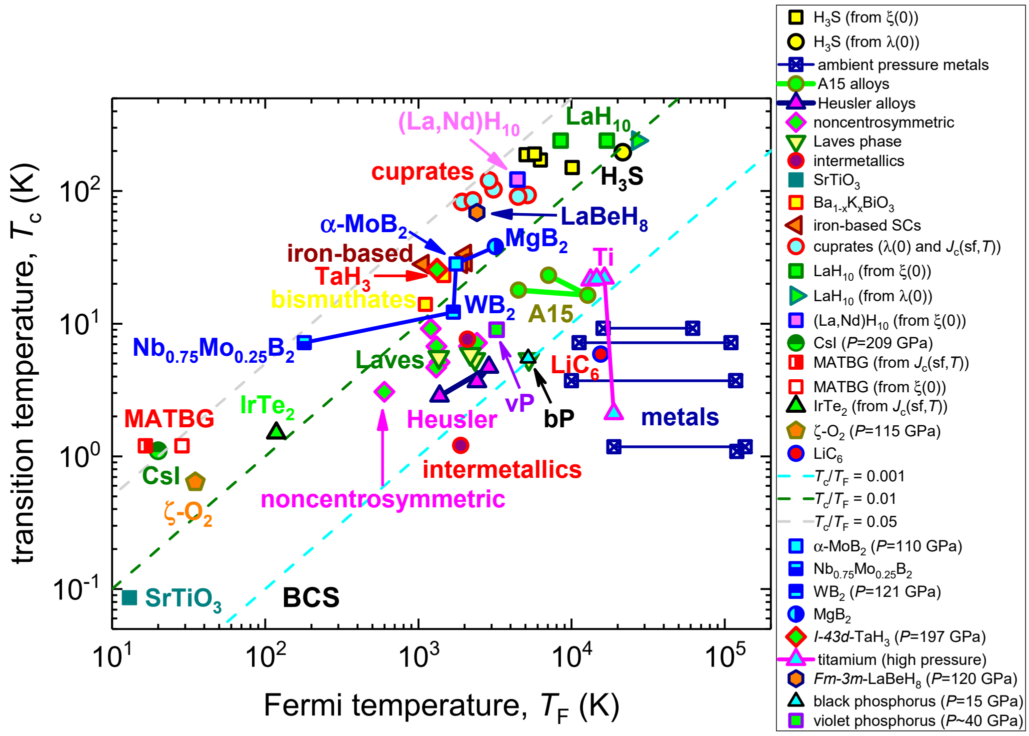

Figure 5. Uemura plot, where highly compressed *Ti*, TaH_3, $LaBeH_8$, black, and violet phosphorous (BP and VP, respectively) are shown together with several families of superconductors: metals, iron-based superconductors, diborides, cuprates, Laves phases, hydrides, and others. References for original data can be found in Refs. [91,101,141,142].

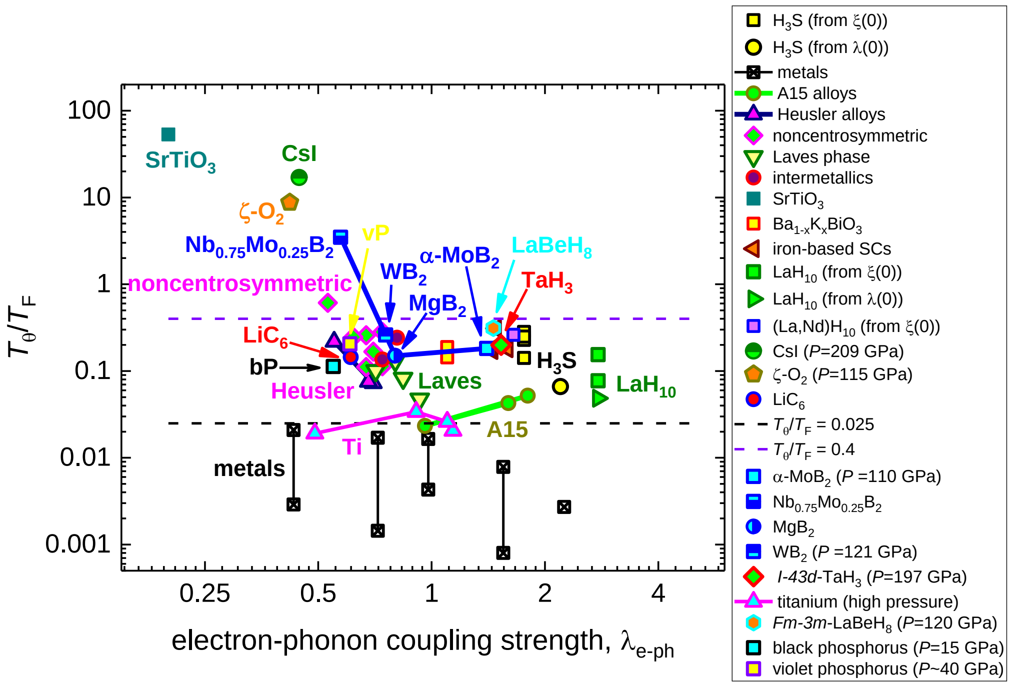

Figure 6. The nonadiabaticity strength constant $\frac{T_\theta}{T_F}$ vs. λ_{e-ph} where several families of superconductors and highly compressed *Ti*, TaH_3, $LaBeH_8$, black, and violet phosphorous are shown. References for original data can be found in Refs. [91,101,141,142].

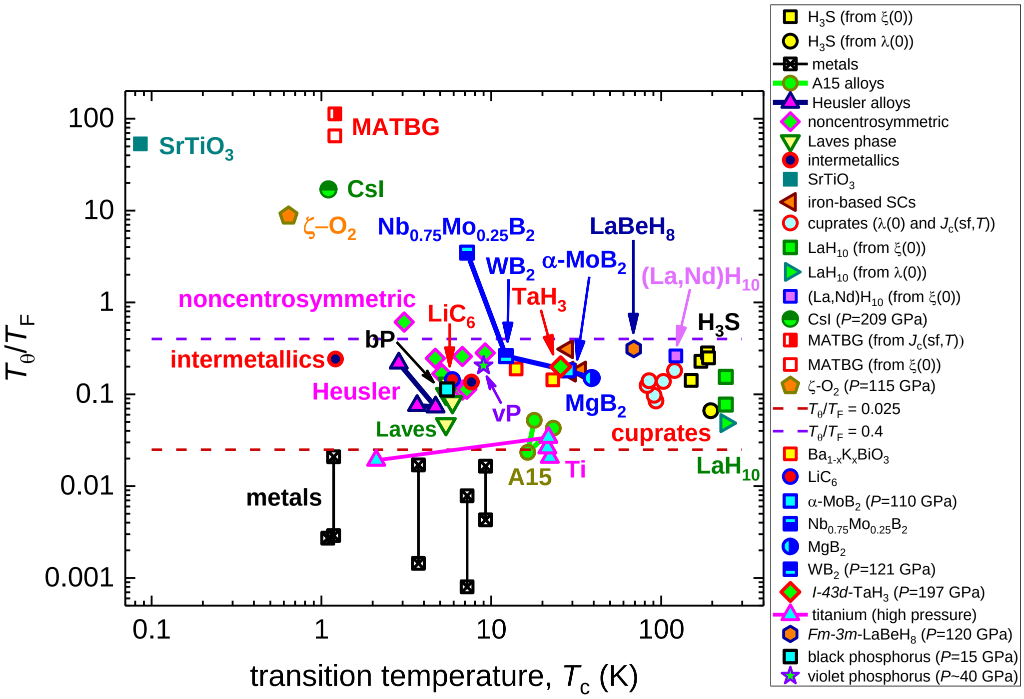

Figure 7. The nonadiabaticity strength constant $\frac{T_\theta}{T_F}$ vs.T_c for several families of superconductors and highly compressed Ti, TaH_3, $LaBeH_8$, black, and violet phosphorous are shown. References for original data can be found in Refs. [91,101,141,142].

3.2. Highly Compressed I-43d-Phase of TaH$_3$

Recently, He et al. [21] reported on the observation of high-temperature superconductivity in the highly compressed *I-43d*-phase of TaH_3. In Figure 8, we show the fit of the $R(T)$ dataset (measured by He et al. [21]) for the tantalum hydride compressed at $P = 197\ GPa$.

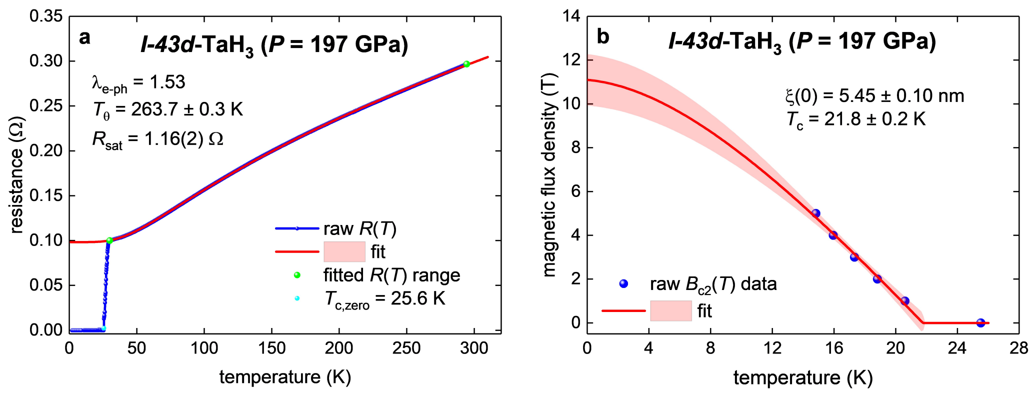

Figure 8. Analyzed experimental data for *I-43d*-phase of TaH_3 at P = 197 GPa (raw data reported by He et al. [21]). (**a**) Temperature-dependent resistance data, $R(T)$, and data fit to Equation (3). Green balls indicate the bounds for which $R(T)$ data were used for the fit to Equation (3). Deduced $T_\theta = (263.7 \pm 0.3)\ K$, $T_{c,zero} = 25.6\ K$, $\lambda_{e-ph} = 1.53$, fit quality is 0.99998. (**b**) The upper critical field data, $B_{c2}(T)$, and data fit to Equation (7). Definition $B_{c2}(T)$ criterion of $\frac{R(T)}{R_{norm}} = 0.02$ was used. Deduced parameters are: $\xi(0) = (2.33 \pm 0.02)\ nm$, $T_c = (21.8 \pm 0.2)\ K$. Fit quality is 0.9943. The pink shadow areas in both panels show 95% confidence bands.

We deduced $\lambda_{e-ph} = 1.53$ (Figure 8) by using Equations (4)–(6). The deduced value was within the ballpark value for other highly compressed hydride superconductors [3,119].

He et al. [21] did not report the result of the Hall coefficient measurements. Based on this, we determined the Fermi temperature using Equation (9). To do this, we deduced the $B_{c2}(T)$ dataset from $R(T,B)$ curves reported by He et al. [21] in their Figure 2a [21]. We defined the $B_{c2}(T)$ using the criterion of $\frac{R(T)}{R_{norm}} = 0.02$. Obtained $B_{c2}(T)$ data and the data fit are shown in Figure 8b. Deduced $\xi(0) = (5.45 \pm 0.10)\ nm$.

To calculate the Fermi temperature in the *I-43d*-phase of TaH_3 at P = 197 GPa, we substituted derived $\lambda_{e-ph} = 1.53$ and $\xi(0) = 5.45\ nm$ in Equation (9), where $\alpha = \frac{2\Delta(0)}{k_B \cdot T_c} = 4.39$ was obtained by substituting $\lambda_{e-ph} = 1.53$ in Equation (10) (Figure 1).

In the result, we determined the following fundamental parameters of the *I-43d*-phase of TaH_3 ($P = 197\ GPa$):

(1) the Debye temperature, $T_\theta = 263\ K$;
(2) the electron–phonon coupling constant, $\lambda_{e-ph} = 1.53 \pm 0.13$;
(3) the ground-state coherence length, $\xi(0) = (1.53 \pm 0.13)\ nm$;
(4) the Fermi temperature, $T_F = (1324\ \pm 74)\ K$;
(5) $\frac{T_c}{T_F} = 0.019 \pm 0.01$, which implies that this phase falls in the unconventional superconductors band in the Uemura plot;
(6) the nonadiabaticity strength constant, $\frac{T_\theta}{T_F} = 0.20 \pm 0.01$.

In Figures 5–7, one can see the position of the *I-43d*-phase of TaH_3 at P = 197 GPa. The position of this hydride in Figures 5–7 confirmed that the TaH_3 is typical superhydride, exhibiting a similar strength of nonadiabatic effects to H_3S and LaH_{10}.

3.3. Highly Compressed Fm-3m-Phase of $LaBeH_8$

Recently, Song et al. [110] reported on the observation of high-temperature superconductivity in highly compressed $LaBeH_8$. The crystalline structure of this superhydride at $P = 120\ GPa$ was identified as $Fm\bar{3}m$. This crystalline structure was predicted by Zhang et al. [143]. Figure 9a shows the fit of the $R(T)$ dataset (measured by Song et al. [110]) in the $LaBeH_8$ compressed at $P = 120\ GPa$.

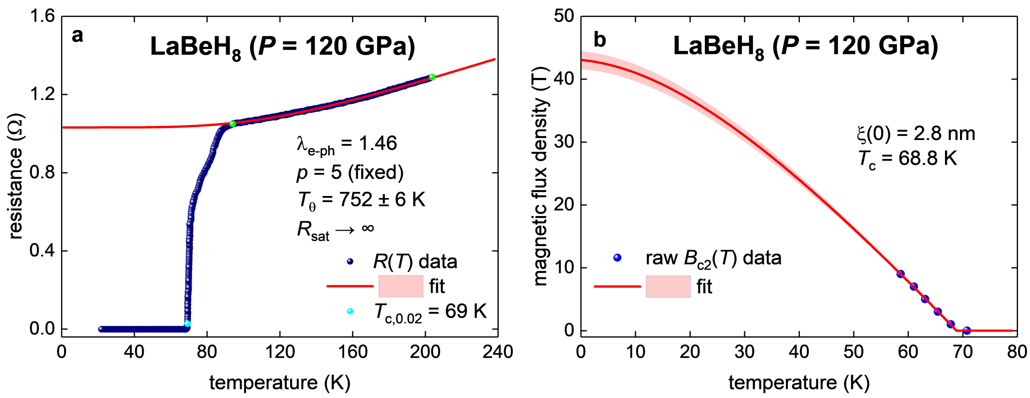

Figure 9. Analyzed experimental data for $Fm\bar{3}m$-phase of $LaBeH_8$ at P = 120 GPa (raw data reported by Song et al. [110]). (**a**) Temperature-dependent resistance data, $R(T)$, and data fit to Equation (3). Green balls indicate the bounds for which $R(T)$ data were used for the fit to Equation (3). Deduced $T_\theta = (752 \pm 6)\ K$, $T_{c,0.02} = 269\ K$, $\lambda_{e-ph} = 1.46$, fit quality is 0.9990. (**b**) The upper critical field data, $B_{c2}(T)$, and data fit to Equation (7). Definition $B_{c2}(T)$ criterion of $\frac{R(T)}{R_{norm}} = 0.25$ was used. Deduced parameters are: $\xi(0) = 2.8\ nm$, $T_c = 68.8\ K$. Fit quality is 0.9995. The pink areas in both panels show 95% confidence bands.

The $B_{c2}(T)$ dataset was extracted from $R(T,B)$ curves reported by Song et al. [110] in their Figure 3a [110]. For the $B_{c2}(T)$ definition, we utilized the criterion of $\frac{R(T)}{R_{norm}} = 0.25$. The obtained $B_{c2}(T)$ data and the data fit are shown in Figure 9b. Deduced $\xi(0) = 2.8\ nm$.

Examining the results of the performed study, we determined that the $Fm\bar{3}m$-phase of $LaBeH_8$ at P = 120 GPa exhibits the following parameters:

(1) the Debye temperature, $T_\theta = (752 \pm 6)\ K$;
(2) the electron–phonon coupling constant, $\lambda_{e-ph} = 1.46$;

(3) the ground-state coherence length, $\xi(0) = (2.80 \pm 0.02)\ nm$;
(4) the Fermi temperature, $T_F = 2413\ K$;
(5) $\frac{T_c}{T_F} = 0.029$, which implies that this phase falls in the unconventional superconductors band in the Uemura plot;
(6) the nonadiabaticity strength constant, $\frac{T_\theta}{T_F} = 0.31 \pm 0.01$.

3.4. Highly Compressed Black Phosphorous

The impact of high pressure on the superconducting parameters of black phosphorous has been studied over several decades [111–114]. Recent detailed studies in this field have been reported by Guo et al. [112], Li et al. [111], and Jin et al. [114].

To show the reliability of high-pressure studies of superconductors (which was recently questioned by non-experts in the field [144,145]), in Figure 10, we show raw $R(T)$ datasets measured at $P = 15\ GPa$ from the two independent research groups of Shirotani et al. [113] and Li et al. [111]. It should be stressed that these reports have been published within a timeframe of 24 years.

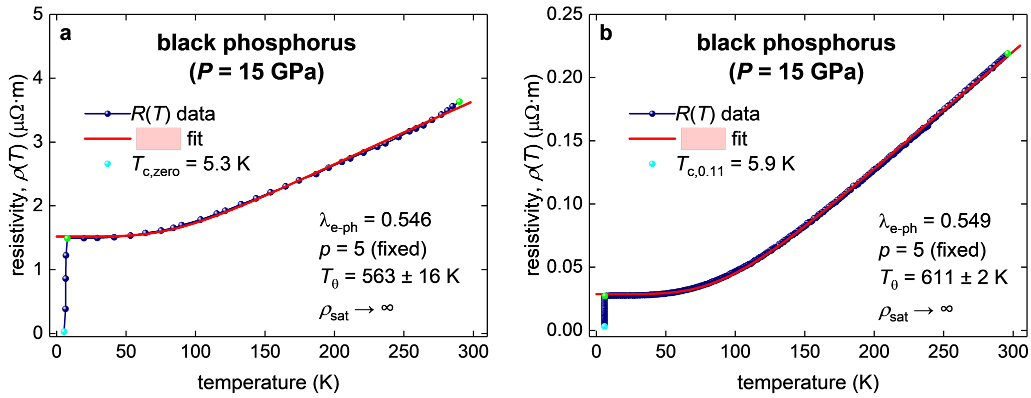

Figure 10. Analysis of experimental $\rho(T)$ datasets for black phosphorus compressed at P = 15 GPa reported by (**a**) Shirotani et al. [113] and by (**b**) Li et al. [111]. Green balls indicate the bounds for which $\rho(T)$ data were used for the fit to Equation (3). Deduced parameters are: (**a**) $T_\theta = (563 \pm 16)\ K$, $T_{c,zerp} = 5.3\ K$, $\lambda_{e-ph} = 0.546$, fit quality is 0.9983; (**b**) $T_\theta = (611 \pm 2)\ K$, $T_{c,zerp} = 5.9\ K$, $\lambda_{e-ph} = 0.549$, fit quality is 0.9998. The pink shadow areas in both panels 95% confidence bands.

The agreement between deduced λ_{e-ph} (Figure 10) from two datasets [111,113] is remarkable. It should be noted that the approach used for our analysis (Figure 10) was developed to analyze data measured in highly compressed near-room-temperature superconductors [119]. This feature implies that several concerns expressed by non-experts in the field [144–147] with regard to highly compressed near-room-temperature hydride superconductors do not have any scientific background.

Figure 11 shows $B_{c2}(T)$ datasets extracted from raw $R(T,B)$ datasets measured at very close pressures, with values of $P = 15.9\ GPa$ [112] (panel a) and $P = 15\ GPa$ [111] (panel b). These two datasets were reported by two independent groups. For the $B_{c2}(T)$ definition, we utilized the same strict criterion of $\frac{R(T)}{R_{norm}} = 0.01$ for both $R(T,B)$ datasets in Figure 11.

The average deduced parameters for black phosphorus $P = 15\ GPa$, which we derived from experimental data analysis reported by three different research groups, are as follows:

(1) the Debye temperature, $T_\theta = 587\ K$;
(2) the electron–phonon coupling constant, $\lambda_{e-ph} = 0.548$;
(3) the ground-state coherence length, $\xi(0) = 77\ nm$;
(4) the Fermi temperature, $T_F = 5200\ K$;
(5) $\frac{T_c}{T_F} = 0.001$, which implies that black phosphorus falls in the conventional superconductors band in the Uemura plot;
(6) the nonadiabaticity strength constant, $\frac{T_\theta}{T_F} = 0.11$.

The deduced parameters show that the black phosphorus at $P = 15\ GPa$ exhibits low-strength nonadiabatic effects.

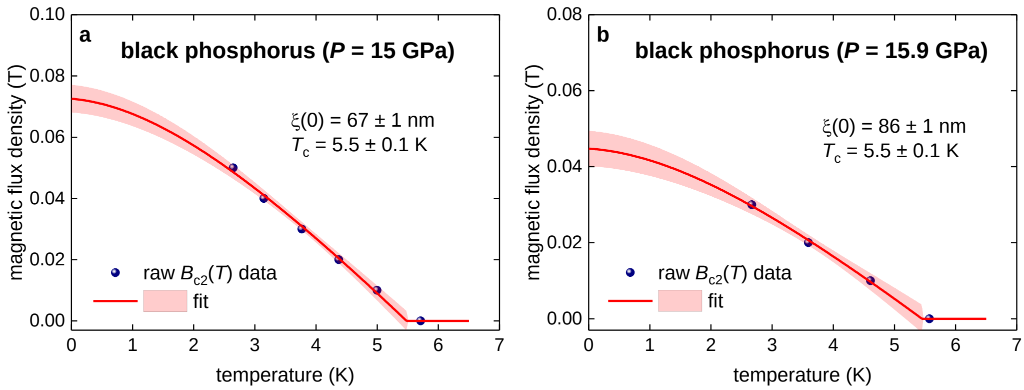

Figure 11. Analysis of experimental $B_{c2}(T)$ datasets for black phosphorus compressed at (**a**) P = 15 GPa reported by Li et al. [111], and (**b**) P = 15.9 GPa reported by Guo et al. [112]. Deduced parameters are: (**a**) $\xi(0) = (67 \pm 1)\ nm$, $T_c = 5.5 \pm 0.1\ K$, fit quality is 0.9965; (**b**) $\xi(0) = (86 \pm 1)\ nm$, $T_c = 5.5 \pm 0.1\ K$, fit quality is 0.9981. Pink shadow areas in both panels show 95% confidence bands are shown.

3.5. Highly Compressed Violet Phosphorous

Recently, Wu et al. [62] reported on the observation of the superconducting state in compressed violet phosphorus (vP). This material exhibits $T_c > 5\ K$ at high pressure in the range of 3.6 $GPa \le P \le 40.2\ GPa$. In Figure 12a, we showed the $R(T)$ dataset (measured by Wu et al. [62]) and fitted data to Equation (3).

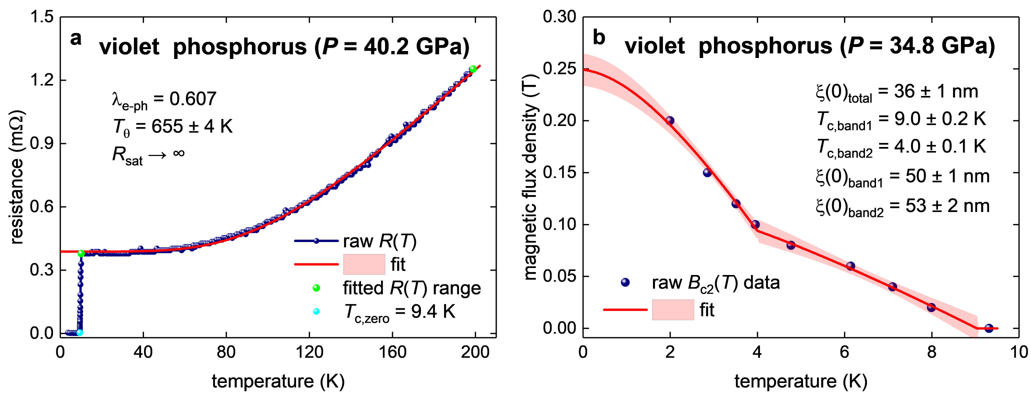

Figure 12. Analysis of experimental data for violet phosphorus compressed at (**a**) $P = 40.2\ GPa$ and (**b**) $P = 34.8\ GPa$. Raw data reported by Wu et al. [62]. (**a**) Temperature-dependent resistance data, $R(T)$, and data fit to Equation (3). Green balls indicate the bounds for which $R(T)$ data were used for the fit to Equation (3). Deduced $T_\theta = (655 \pm 4\ )K$, $T_{c,0.01} = 9.4\ K$, $\lambda_{e-ph} = 0.607$, fit quality is 0.9991. (**b**) The upper critical field data, $B_{c2}(T)$, and data fit to Equation (13). Definition $B_{c2}(T)$ criterion of $\frac{R(T)}{R_{norm}} = 0.14$ was used. The deduced parameters are: $\xi(0)_{band1} = (50 \pm 1)\ nm$, $T_{c,band1} = (9.0\ \pm 0.2)\ K$, $\xi(0)_{band1} = (53 \pm 2)\ nm$, $T_{c,band2} = (4.0\ \pm 0.1)\ K$. Fit quality is 0.9977. The pink areas in both panels show 95% confidence bands.

The $B_{c2}(T)$ dataset was extracted from the only $R(T,B)$ dataset reported by Wu et al. [62] for material compressed at $P = 34.8\ GPa$ [62]. The $B_{c2}(T)$ was defined by the criterion of $\frac{R(T)}{R_{norm}} = 0.14$. The deduced $B_{c2}(T)$ dataset is shown in Figure 12b. Equation (7) does not fit the $B_{c2}(T)$ data well because the $B_{c2}(T)$ goes up at $T \lesssim 4\ K$. We think this means a second band opens up, so we used a two-band model to fit the data [141,148]:

$$B_{c2,total}(T) = B_{c2,band1}(T) + B_{c2,band2}(T), \tag{13}$$

where $B_{c2,band1}(T)$, and $B_{c2,band2}(T)$ exhibit their independent transition temperature and the coherence length. We list deduced values in the figure caption to Figure 12. However, for further analysis, we used $T_c = T_{c,band1} = 9.0\ K$, and $\xi(0)_{total} = (36 \pm 1\ )nm$.

In the result, we derived the following parameters for violet phosphorus comrpessed at $P \sim 40\ GPa$:

(1) the Debye temperature, $T_\theta = (665 \pm 4)\ K$;
(2) the electron–phonon coupling constant, $\lambda_{e-ph} = 0.607$;
(3) the ground-state coherence length, $\xi(0) = (36 \pm 1)\ nm$;
(4) the Fermi temperature, $T_F = 3240\ K$;
(5) $\frac{T_c}{T_F} = 0.003$, which implies that this phase falls near the conventional superconductors band in the Uemura plot;
(6) the nonadiabaticity strength constant, $\frac{T_\theta}{T_F} = 0.21$.

We concluded, that nonadiabatic effects in violet phosphorus compressed at $P \sim 40\ GPa$ are like those in H_3S and LaH_{10} near-room-temperature superconductors.

4. Discussion

As we mentioned, above superconductors can be classified by the ratio of maximum phonon energy, $\hbar\omega_D$ (where ω_D is Debye frequency) to the charge carrier energy at the Fermi level, $\frac{\hbar\omega_D}{k_B T_F}$. For practical use, it is more convenient to replace the $\hbar\omega_D$ with $k_B T_\theta$, where T_θ is the Debye temperature.

Thus, in the adiabatic regime, $\frac{\hbar\omega_D}{k_B T_F} = \frac{T_\theta}{T_F} \lesssim 10^{-3}$, superconductors have fast charge carriers and slow phonons. This condition is satisfied for pure metals and some superconducting alloys (Figures 5–7).

However, as can be seen in Figures 6 and 7, more than $\frac{3}{4}$ of superconductors (including important for practical use Nb_3Sn, MgB_2, pnictides, cuprates, and record-high T_c near-room-temperature superconducting hydrides) have the ratio in a different range [91,101]:

$$0.025 \leq \frac{\hbar\omega_D}{k_B T_F} \leq 0.4, \tag{14}$$

Our experimental data search [70,80] revealed that only six superconductors exhibit (Figures 6 and 7):

$$\frac{\hbar\omega_D}{k_B T_F} > 0.4. \tag{15}$$

These materials are [91,101]: $Nb_{0.75}Mo_{0.25}B_2$ and $Nb_{0.5}Os_{0.5}$, which are highly compressed metalized oxygen; magic-angle twisted bilayer graphene $SrTiO_3$; and highly compressed metalized ionic salt, CsI. It should be stressed that all these superconductors exhibit low transition temperatures, $T_c < 8\ K$.

The five recently discovered superconductors (Sections 3.1–3.5) studied in this report confirmed the validity of Equation (14). And, thus, perhaps a deep physical origin related to the strength of the nonadiabaticity $\frac{\hbar\omega_D}{k_B T_F} = \frac{T_\theta}{T_F}$ within the range indicated in Equation (14) can be revealed.

Nonadiabatic effects are crucial in reducing the superconducting transition temperature to well below the value predicted by classical (BCS-Eliashberg) theories of electron–phonon-mediated superconductivity [93,115]. This understanding was first reported by Pietronero and co-workers [103–105,107]. It can be seen in Figure 7 that materials with the highest strength of nonadiabaticity $\frac{T_\theta}{T_F}$ (for instance, $SrTiO_3$ and magic-angle twisted bilayer graphene) exhibit the superconducting transition temperature $T_c \lesssim 1\ K$, while all materials with $T_c \gtrsim 35\ K$ exhibit $\frac{T_\theta}{T_F}$ within a range indicated by Equation (14).

5. Conclusions

In this work, we analyzed experimental data for five new highly compressed superconductors: $\delta - Ti$ [63,64], TaH_3 [21], $LaBeH_8$ [110], black phosphorous [111–113], and violet phosphorous [62]. We established several superconducting parameters for these superconductors, including the strength of nonadiabaticity, $\frac{\hbar\omega_D}{k_B T_F} = \frac{T_\theta}{T_F}$.

Funding: This research was funded by the Ministry of Science and Higher Education of the Russian Federation, grant number No. 122021000032-5 (theme "Pressure"). The research funding from the Ministry of Science and Higher Education of the Russian Federation (Ural Federal University Program of Development within the Priority-2030 Program) is gratefully acknowledged.

Data Availability Statement: Not applicable.

Conflicts of Interest: The author declares no conflict of interest. The funders had no role in the design of the study; in the collection, analyses, or interpretation of data; in the writing of the manuscript; or in the decision to publish the results.

References

1. Drozdov, A.P.; Eremets, M.I.; Troyan, I.A.; Ksenofontov, V.; Shylin, S.I. Conventional Superconductivity at 203 Kelvin at High Pressures in the Sulfur Hydride System. *Nature* **2015**, *525*, 73–76. [CrossRef] [PubMed]
2. Duan, D.; Liu, Y.; Tian, F.; Li, D.; Huang, X.; Zhao, Z.; Yu, H.; Liu, B.; Tian, W.; Cui, T. Pressure-Induced Metallization of Dense (H2S)2H2 with High-Tc Superconductivity. *Sci. Rep.* **2014**, *4*, 6968. [CrossRef] [PubMed]
3. Lilia, B.; Hennig, R.; Hirschfeld, P.; Profeta, G.; Sanna, A.; Zurek, E.; Pickett, W.E.; Amsler, M.; Dias, R.; Eremets, M.I.; et al. The 2021 Room-Temperature Superconductivity Roadmap. *J. Phys. Condens. Matter* **2022**, *34*, 183002. [CrossRef] [PubMed]
4. Li, Y.; Hao, J.; Liu, H.; Li, Y.; Ma, Y. The Metallization and Superconductivity of Dense Hydrogen Sulfide. *J. Chem. Phys.* **2014**, *140*, 174712. [CrossRef]
5. Sun, D.; Minkov, V.S.; Mozaffari, S.; Sun, Y.; Ma, Y.; Chariton, S.; Prakapenka, V.B.; Eremets, M.I.; Balicas, L.; Balakirev, F.F. High-Temperature Superconductivity on the Verge of a Structural Instability in Lanthanum Superhydride. *Nat. Commun.* **2021**, *12*, 6863. [CrossRef]
6. Ma, L.; Wang, K.; Xie, Y.; Yang, X.; Wang, Y.; Zhou, M.; Liu, H.; Yu, X.; Zhao, Y.; Wang, H.; et al. High-Temperature Superconducting Phase in Clathrate Calcium Hydride CaH6 up to 215 K at a Pressure of 172 GPa. *Phys. Rev. Lett.* **2022**, *128*, 167001. [CrossRef]
7. Wang, H.; Tse, J.S.; Tanaka, K.; Iitaka, T.; Ma, Y. Superconductive Sodalite-like Clathrate Calcium Hydride at High Pressures. *Proc. Natl. Acad. Sci. USA* **2012**, *109*, 6463–6466. [CrossRef]
8. Bi, J.; Nakamoto, Y.; Zhang, P.; Shimizu, K.; Zou, B.; Liu, H.; Zhou, M.; Liu, G.; Wang, H.; Ma, Y. Giant Enhancement of Superconducting Critical Temperature in Substitutional Alloy (La,Ce)H_9. *Nat. Commun.* **2022**, *13*, 5952. [CrossRef]
9. Du, M.; Song, H.; Zhang, Z.; Duan, D.; Cui, T. Room-Temperature Superconductivity in Yb/Lu Substituted Clathrate Hexahydrides under Moderate Pressure. *Research* **2022**, *2022*, 9784309. [CrossRef]
10. Alarco, J.A.; Almutairi, A.; Mackinnon, I.D.R. Progress Towards a Universal Approach for Prediction of the Superconducting Transition Temperature. *J. Supercond. Nov. Magn.* **2020**, *33*, 2287–2292. [CrossRef]
11. Kostrzewa, M.; Szczęśniak, K.M.; Durajski, A.P.; Szczęśniak, R. From LaH10 to Room–Temperature Superconductors. *Sci. Rep.* **2020**, *10*, 1592. [CrossRef]
12. Drozdov, A.P.; Kong, P.P.; Minkov, V.S.; Besedin, S.P.; Kuzovnikov, M.A.; Mozaffari, S.; Balicas, L.; Balakirev, F.F.; Graf, D.E.; Prakapenka, V.B.; et al. Superconductivity at 250 K in Lanthanum Hydride under High Pressures. *Nature* **2019**, *569*, 528–531. [CrossRef] [PubMed]
13. Somayazulu, M.; Ahart, M.; Mishra, A.K.; Geballe, Z.M.; Baldini, M.; Meng, Y.; Struzhkin, V.V.; Hemley, R.J. Evidence for Superconductivity above 260 K in Lanthanum Superhydride at Megabar Pressures. *Phys. Rev. Lett.* **2019**, *122*, 027001. [CrossRef] [PubMed]
14. Semenok, D.V.; Kvashnin, A.G.; Ivanova, A.G.; Svitlyk, V.; Fominski, V.Y.; Sadakov, A.V.; Sobolevskiy, O.A.; Pudalov, V.M.; Troyan, I.A.; Oganov, A.R. Superconductivity at 161 K in Thorium Hydride ThH_{10}: Synthesis and Properties. *Mater. Today* **2020**, *33*, 36–44. [CrossRef]
15. Troyan, I.A.; Semenok, D.V.; Kvashnin, A.G.; Sadakov, A.V.; Sobolevskiy, O.A.; Pudalov, V.M.; Ivanova, A.G.; Prakapenka, V.B.; Greenberg, E.; Gavriliuk, A.G.; et al. Anomalous High-Temperature Superconductivity in YH_6. *Adv. Mater.* **2021**, *33*, 2006832. [CrossRef]
16. Semenok, D.V.; Troyan, I.A.; Ivanova, A.G.; Kvashnin, A.G.; Kruglov, I.A.; Hanfland, M.; Sadakov, A.V.; Sobolevskiy, O.A.; Pervakov, K.S.; Lyubutin, I.S.; et al. Superconductivity at 253 K in Lanthanum–Yttrium Ternary Hydrides. *Mater. Today* **2021**, *48*, 18–28. [CrossRef]
17. Kong, P.; Minkov, V.S.; Kuzovnikov, M.A.; Drozdov, A.P.; Besedin, S.P.; Mozaffari, S.; Balicas, L.; Balakirev, F.F.; Prakapenka, V.B.; Chariton, S.; et al. Superconductivity up to 243 K in the Yttrium-Hydrogen System under High Pressure. *Nat. Commun.* **2021**, *12*, 5075. [CrossRef]

18. Zhang, C.; He, X.; Li, Z.; Zhang, S.; Feng, S.; Wang, X.; Yu, R.; Jin, C. Superconductivity in Zirconium Polyhydrides with Tc above 70 K. *Sci. Bull.* **2022**, *67*, 907–909. [CrossRef]
19. Zhang, C.L.; He, X.; Li, Z.W.; Zhang, S.J.; Min, B.S.; Zhang, J.; Lu, K.; Zhao, J.F.; Shi, L.C.; Peng, Y.; et al. Superconductivity above 80 K in Polyhydrides of Hafnium. *Mater. Today Phys.* **2022**, *27*, 100826. [CrossRef]
20. Minkov, V.S.; Prakapenka, V.B.; Greenberg, E.; Eremets, M.I. A Boosted Critical Temperature of 166 K in Superconducting D_3S Synthesized from Elemental Sulfur and Hydrogen. *Angew. Chem.* **2020**, *132*, 19132–19136. [CrossRef]
21. He, X.; Zhang, C.L.; Li, Z.W.; Zhang, S.J.; Min, B.S.; Zhang, J.; Lu, K.; Zhao, J.F.; Shi, L.C.; Peng, Y.; et al. Superconductivity Observed in Tantalum Polyhydride at High Pressure. *Chin. Phys. Lett.* **2023**, *40*, 057404. [CrossRef]
22. Minkov, V.S.; Bud'ko, S.L.; Balakirev, F.F.; Prakapenka, V.B.; Chariton, S.; Husband, R.J.; Liermann, H.P.; Eremets, M.I. Magnetic Field Screening in Hydrogen-Rich High-Temperature Superconductors. *Nat. Commun.* **2022**, *13*, 3194. [CrossRef] [PubMed]
23. Minkov, V.S.; Ksenofontov, V.; Bud'ko, S.L.; Talantsev, E.F.; Eremets, M.I. Magnetic Flux Trapping in Hydrogen-Rich High-Temperature Superconductors. *Nat. Phys.* 2023, *online ahead of print*. [CrossRef]
24. Troyan, I.A.; Semenok, D.V.; Ivanova, A.G.; Sadakov, A.V.; Zhou, D.; Kvashnin, A.G.; Kruglov, I.A.; Sobolevskiy, O.A.; Lyubutina, M.V.; Perekalin, D.S.; et al. Non-Fermi-Liquid Behavior of Superconducting SnH_4. *arXiv* **2023**, arXiv:2303.06339. [CrossRef]
25. Flores-Livas, J.A.; Boeri, L.; Sanna, A.; Profeta, G.; Arita, R.; Eremets, M. A Perspective on Conventional High-Temperature Superconductors at High Pressure: Methods and Materials. *Phys. Rep.* **2020**, *856*, 1–78. [CrossRef]
26. Bhattacharyya, P.; Chen, W.; Huang, X.; Chatterjee, S.; Huang, B.; Kobrin, B.; Lyu, Y.; Smart, T.J.; Block, M.; Wang, E.; et al. Imaging the Meissner Effect and Flux Trapping in a Hydride Superconductor at Megabar Pressures Using a Nanoscale Quantum Sensor. *arXiv* **2023**, arXiv:2306.03122. [CrossRef]
27. Goh, S.K.; Zhang, W.; Yip, K.Y. Trapped Magnetic Flux in Superconducting Hydrides. *Nat. Phys.* 2023, *online ahead of print*. [CrossRef]
28. Ho, K.O.; Leung, M.Y.; Wang, W.; Xie, J.; Yip, K.Y.; Wu, J.; Goh, S.K.; Denisenko, A.; Wrachtrup, J.; Yang, S. Spectroscopic Study of N-V Sensors in Diamond-Based High-Pressure Devices. *Phys. Rev. Appl.* **2023**, *19*, 044091. [CrossRef]
29. Ho, K.O.; Leung, M.Y.; Reddy, P.; Xie, J.; Wong, K.C.; Jiang, Y.; Zhang, W.; Yip, K.Y.; Leung, W.K.; Pang, Y.Y.; et al. Probing the Evolution of the Electron Spin Wave Function of the Nitrogen-Vacancy Center in Diamond via Pressure Tuning. *Phys. Rev. Appl.* **2022**, *18*, 064042. [CrossRef]
30. Ho, K.O.; Leung, M.Y.; Jiang, Y.; Ao, K.P.; Zhang, W.; Yip, K.Y.; Pang, Y.Y.; Wong, K.C.; Goh, S.K.; Yang, S. Probing Local Pressure Environment in Anvil Cells with Nitrogen-Vacancy ($N\text{-}V^-$) Centers in Diamond. *Phys. Rev. Appl.* **2020**, *13*, 024041. [CrossRef]
31. Yip, K.Y.; Ho, K.O.; Yu, K.Y.; Chen, Y.; Zhang, W.; Kasahara, S.; Mizukami, Y.; Shibauchi, T.; Matsuda, Y.; Goh, S.K.; et al. Measuring Magnetic Field Texture in Correlated Electron Systems under Extreme Conditions. *Science* **2019**, *366*, 1355–1359. [CrossRef]
32. Sakata, M.; Einaga, M.; Dezhong, M.; Sato, T.; Orimo, S.; Shimizu, K. Superconductivity of Lanthanum Hydride Synthesized Using AlH_3 as a Hydrogen Source. *Supercond. Sci. Technol.* **2020**, *33*, 114004. [CrossRef]
33. Mozaffari, S.; Sun, D.; Minkov, V.S.; Drozdov, A.P.; Knyazev, D.; Betts, J.B.; Einaga, M.; Shimizu, K.; Eremets, M.I.; Balicas, L.; et al. Superconducting Phase Diagram of H_3S under High Magnetic Fields. *Nat. Commun.* **2019**, *10*, 2522. [CrossRef]
34. Chen, W.; Semenok, D.V.; Kvashnin, A.G.; Huang, X.; Kruglov, I.A.; Galasso, M.; Song, H.; Duan, D.; Goncharov, A.F.; Prakapenka, V.B.; et al. Synthesis of Molecular Metallic Barium Superhydride: Pseudocubic BaH_{12}. *Nat. Commun.* **2021**, *12*, 273. [CrossRef] [PubMed]
35. Zhou, D.; Semenok, D.V.; Duan, D.; Xie, H.; Chen, W.; Huang, X.; Li, X.; Liu, B.; Oganov, A.R.; Cui, T. Superconducting Praseodymium Superhydrides. *Sci. Adv.* **2020**, *6*, 1–9. [CrossRef] [PubMed]
36. Hong, F.; Shan, P.F.; Yang, L.X.; Yue, B.B.; Yang, P.T.; Liu, Z.Y.; Sun, J.P.; Dai, J.H.; Yu, H.; Yin, Y.Y.; et al. Possible Superconductivity at ~70 K in Tin Hydride SnHx under High Pressure. *Mater. Today Phys.* **2022**, *22*, 100596. [CrossRef]
37. Li, Z.; He, X.; Zhang, C.; Lu, K.; Min, B.; Zhang, J.; Zhang, S.; Zhao, J.; Shi, L.; Peng, Y.; et al. Superconductivity above 70 K Observed in Lutetium Polyhydrides. *Sci. China Phys. Mech. Astron.* **2023**, *66*, 267411. [CrossRef]
38. Chen, W.; Semenok, D.V.; Huang, X.; Shu, H.; Li, X.; Duan, D.; Cui, T.; Oganov, A.R. High-Temperature Superconducting Phases in Cerium Superhydride with T_c up to 115 K below a Pressure of 1 Megabar. *Phys. Rev. Lett.* **2021**, *127*, 117001. [CrossRef] [PubMed]
39. Semenok, D.V.; Troyan, I.A.; Sadakov, A.V.; Zhou, D.; Galasso, M.; Kvashnin, A.G.; Ivanova, A.G.; Kruglov, I.A.; Bykov, A.A.; Terent'ev, K.Y.; et al. Effect of Magnetic Impurities on Superconductivity in LaH_{10}. *Adv. Mater.* **2022**, *34*, 2204038. [CrossRef]
40. Li, Z.; He, X.; Zhang, C.; Wang, X.; Zhang, S.; Jia, Y.; Feng, S.; Lu, K.; Zhao, J.; Zhang, J.; et al. Superconductivity above 200 K Discovered in Superhydrides of Calcium. *Nat. Commun.* **2022**, *13*, 2863. [CrossRef]
41. Chen, W.; Huang, X.; Semenok, D.V.; Chen, S.; Zhou, D.; Zhang, K.; Oganov, A.R.; Cui, T. Enhancement of Superconducting Properties in the La–Ce–H System at Moderate Pressures. *Nat. Commun.* **2023**, *14*, 2660. [CrossRef]
42. Purans, J.; Menushenkov, A.P.; Besedin, S.P.; Ivanov, A.A.; Minkov, V.S.; Pudza, I.; Kuzmin, A.; Klementiev, K.V.; Pascarelli, S.; Mathon, O.; et al. Local Electronic Structure Rearrangements and Strong Anharmonicity in YH_3 under Pressures up to 180 GPa. *Nat. Commun.* **2021**, *12*, 1765. [CrossRef]
43. Shao, M.; Chen, W.; Zhang, K.; Huang, X.; Cui, T. High-Pressure Synthesis of Superconducting Clathratelike YH_4. *Phys. Rev. B* **2021**, *104*, 174509. [CrossRef]

44. Guo, J.; Shutov, G.; Chen, S.; Wang, Y.; Zhou, D.; Cui, T.; Huang, X.; Semenok, D. Stabilization of High-Temperature Superconducting A15 Phase La_4H_{23} below 100 GPa. *arXiv* **2023**, arXiv:2307.13067. [CrossRef]
45. Sadakov, A.V.; Vlasenko, V.A.; Troyan, I.A.; Sobolevskiy, O.A.; Semenok, D.V.; Zhou, D.; Pudalov, V.M. Vortex Phase Dynamics in Yttrium Superhydride YH_6 at Megabar Pressures. *J. Phys. Chem. Lett.* **2023**, *14*, 6666–6671. [CrossRef] [PubMed]
46. Liu, W.; Wang, E.; Chen, G.; Zhu, X.; Zhang, Y.; Sheng, Y.; Wen, H.-H. Absence of Superconductivity in $LiPdH_X$. *Philos. Mag.* **2018**, *98*, 623–631. [CrossRef]
47. Zhang, Y.; Liu, W.; Zhu, X.; Zhao, H.; Hu, Z.; He, C.; Wen, H.-H. Unprecedented High Irreversibility Line in the Nontoxic Cuprate Superconductor $(Cu,C)Ba_2Ca_3Cu_4O_{11+\delta}$. *Sci. Adv.* **2018**, *4*, eaau0192. [CrossRef]
48. He, C.; Ming, X.; Si, J.; Zhu, X.; Wang, J.; Wen, H.-H. Characterization of the $(Cu,C)Ba_2Ca_3Cu_4O_{11+\delta}$ Single Crystals Grown under High Pressure. *Supercond. Sci. Technol.* **2022**, *35*, 025004. [CrossRef]
49. Zhou, Y.; Guo, J.; Cai, S.; Zhao, J.; Gu, G.; Lin, C.; Yan, H.; Huang, C.; Yang, C.; Long, S.; et al. Quantum Phase Transition from Superconducting to Insulating-like State in a Pressurized Cuprate Superconductor. *Nat. Phys.* **2022**, *18*, 406–410. [CrossRef]
50. Adachi, S.; Matsumoto, R.; Hara, H.; Saito, Y.; Song, P.; Takeya, H.; Watanabe, T.; Takano, Y. Pressure Effect in Bi-2212 and Bi-2223 Cuprate Superconductor. *Appl. Phys. Express* **2019**, *12*, 043002. [CrossRef]
51. Mark, A.C.; Campuzano, J.C.; Hemley, R.J. Progress and Prospects for Cuprate High Temperature Superconductors under Pressure. *High Press. Res.* **2022**, *42*, 137–199. [CrossRef]
52. Yamamoto, A.; Takeshita, N.; Terakura, C.; Tokura, Y. High Pressure Effects Revisited for the Cuprate Superconductor Family with Highest Critical Temperature. *Nat. Commun.* **2015**, *6*, 8990. [CrossRef]
53. Mariappan, S.; Bhoi, D.; Krishnan, M.; Shoko, N.; Vajeeston, P.; Arushi; Kushwaha, R.K.; Singh, R.P.; Sonachalam, A.; Uwatoko, Y. Electronic Properties of α-Mn-Type Non-Centrosymmetric Superconductor $Re_{5.5}Ta$ under Hydrostatic Pressure. *Supercond. Sci. Technol.* **2023**, *36*, 025002. [CrossRef]
54. Lim, J.; Hire, A.C.; Quan, Y.; Kim, J.S.; Xie, S.R.; Sinha, S.; Kumar, R.S.; Popov, D.; Park, C.; Hemley, R.J.; et al. Creating Superconductivity in WB_2 through Pressure-Induced Metastable Planar Defects. *Nat. Commun.* **2022**, *13*, 7901. [CrossRef] [PubMed]
55. Pei, C.; Zhang, J.; Wang, Q.; Zhao, Y.; Gao, L.; Gong, C.; Tian, S.; Luo, R.; Li, M.; Yang, W.; et al. Pressure-Induced Superconductivity at 32 K in MoB_2. *Natl. Sci. Rev.* **2023**, *10*, nwad034. [CrossRef] [PubMed]
56. Li, C.; Su, Y.; Zhang, C.; Pei, C.; Cao, W.; Wang, Q.; Zhao, Y.; Gao, L.; Zhu, S.; Zhang, M.; et al. Pressure-Tuning Superconductivity in Noncentrosymmetric Topological Materials ZrRuAs. *Materials* **2022**, *15*, 7694. [CrossRef] [PubMed]
57. Pei, C.; Zhang, J.; Gong, C.; Wang, Q.; Gao, L.; Zhao, Y.; Tian, S.; Cao, W.; Li, C.; Lu, Z.-Y.; et al. Distinct Superconducting Behaviors of Pressurized WB_2 and ReB_2 with Different Local B Layers. *Sci. China Phys. Mech. Astron.* **2022**, *65*, 287412. [CrossRef]
58. Zamyatin, D.A.; Pankrushina, E.A.; Streltsov, S.V.; Ponosov, Y.S. Pressure-Induced Reversible Local Structural Disorder in Superconducting $AuAgTe_4$. *Inorganics* **2023**, *11*, 99. [CrossRef]
59. Liu, Z.Y.; Dong, Q.X.; Yang, P.T.; Shan, P.F.; Wang, B.S.; Sun, J.P.; Dun, Z.L.; Uwatoko, Y.; Chen, G.F.; Dong, X.L.; et al. Pressure-Induced Superconductivity up to 9 K in the Quasi-One-Dimensional KMn_6Bi_5. *Phys. Rev. Lett.* **2022**, *128*, 187001. [CrossRef]
60. Shimizu, K. Superconducting Elements under High Pressure. *Phys. C Supercond. Its Appl.* **2018**, *552*, 30–33. [CrossRef]
61. Zhang, H.; Zhong, W.; Meng, Y.; Yue, B.; Yu, X.; Wang, J.-T.; Hong, F. Superconductivity above 12 K with Possible Multiband Features in CsCl-Type PbS. *Phys. Rev. B* **2023**, *107*, 174502. [CrossRef]
62. Wu, Y.Y.; Mu, L.; Zhang, X.; Dai, D.Z.; Xin, L.; Kong, X.M.; Huang, S.Y.; Meng, K.; Yang, X.F.; Tu, C.P.; et al. Pressure-Induced Superconductivity in the van Der Waals Semiconductor Violet Phosphorus. *arXiv* **2023**, arXiv:2307.02989. [CrossRef]
63. Zhang, C.; He, X.; Liu, C.; Li, Z.; Lu, K.; Zhang, S.; Feng, S.; Wang, X.; Peng, Y.; Long, Y.; et al. Record High Tc Element Superconductivity Achieved in Titanium. *Nat. Commun.* **2022**, *13*, 5411. [CrossRef] [PubMed]
64. Liu, X.; Jiang, P.; Wang, Y.; Li, M.; Li, N.; Zhang, Q.; Wang, Y.; Li, Y.-L.; Yang, W. T_c up to 23.6 K and Robust Superconductivity in the Transition Metal δ-Ti Phase at Megabar Pressure. *Phys. Rev. B* **2022**, *105*, 224511. [CrossRef]
65. Ying, J.; Liu, S.; Lu, Q.; Wen, X.; Gui, Z.; Zhang, Y.; Wang, X.; Sun, J.; Chen, X. Record High 36 K Transition Temperature to the Superconducting State of Elemental Scandium at a Pressure of 260 GPa. *Phys. Rev. Lett.* **2023**, *130*, 256002. [CrossRef] [PubMed]
66. He, X.; Zhang, C.; Li, Z.; Liu, C.; Feng, S.; Zhao, J.; Bin, K.L.B.; Zhang, S.; Peng, Y.; Wang, X.; et al. Superconductivity above 30 K Achieved in Dense Scandium. *arXiv* **2023**, arXiv:2303.01062. [CrossRef]
67. Sun, H.; Huo, M.; Hu, X.; Li, J.; Liu, Z.; Han, Y.; Tang, L.; Mao, Z.; Yang, P.; Wang, B.; et al. Signatures of Superconductivity near 80 K in a Nickelate under High Pressure. *Nature* 2023, *online ahead of print*. [CrossRef]
68. Hou, J.; Yang, P.T.; Liu, Z.Y.; Li, J.Y.; Shan, P.F.; Ma, L.; Wang, G.; Wang, N.N.; Guo, H.Z.; Sun, J.P.; et al. Emergence of High-Temperature Superconducting Phase in the Pressurized $La_3Ni_2O_7$ Crystals. *arXiv* **2023**, arXiv:2307.09865. [CrossRef]
69. Zhang, Y.; Su, D.; Huang, Y.; Sun, H.; Huo, M.; Shan, Z.; Ye, K.; Yang, Z.; Li, R.; Smidman, M.; et al. High-Temperature Superconductivity with Zero-Resistance and Strange Metal Behavior in $La_3Ni_2O_7$. *arXiv* **2023**, arXiv:2307.14819. [CrossRef]
70. Errea, I.; Belli, F.; Monacelli, L.; Sanna, A.; Koretsune, T.; Tadano, T.; Bianco, R.; Calandra, M.; Arita, R.; Mauri, F.; et al. Quantum Crystal Structure in the 250-Kelvin Superconducting Lanthanum Hydride. *Nature* **2020**, *578*, 66–69. [CrossRef]
71. Meninno, A.; Errea, I. Ab Initio Study of Metastable Occupation of Tetrahedral Sites in Palladium Hydrides and Its Impact on Superconductivity. *Phys. Rev. B* **2023**, *107*, 024504. [CrossRef]
72. Meninno, A.; Errea, I. Absence of Sizable Superconductivity in Hydrogen Boride: A First-Principles Study. *Phys. Rev. B* **2022**, *106*, 214508. [CrossRef]

73. Belli, F.; Novoa, T.; Contreras-García, J.; Errea, I. Strong Correlation between Electronic Bonding Network and Critical Temperature in Hydrogen-Based Superconductors. *Nat. Commun.* **2021**, *12*, 5381. [CrossRef]
74. Pickard, C.J.; Errea, I.; Eremets, M.I. Superconducting Hydrides under Pressure. *Annu. Rev. Condens. Matter Phys.* **2020**, *11*, 57–76. [CrossRef]
75. Errea, I. Superconducting Hydrides on a Quantum Landscape. *J. Phys. Condens. Matter* **2022**, *34*, 231501. [CrossRef] [PubMed]
76. Hou, P.; Belli, F.; Bianco, R.; Errea, I. Strong Anharmonic and Quantum Effects in *Pm*3*n* AlH_3 under High Pressure: A First-Principles Study. *Phys. Rev. B* **2021**, *103*, 134305. [CrossRef]
77. Errea, I.; Calandra, M.; Pickard, C.J.; Nelson, J.; Needs, R.J.; Li, Y.; Liu, H.; Zhang, Y.; Ma, Y.; Mauri, F. High-Pressure Hydrogen Sulfide from First Principles: A Strongly Anharmonic Phonon-Mediated Superconductor. *Phys. Rev. Lett.* **2015**, *114*, 157004. [CrossRef]
78. Errea, I.; Calandra, M.; Pickard, C.J.; Nelson, J.R.; Needs, R.J.; Li, Y.; Liu, H.; Zhang, Y.; Ma, Y.; Mauri, F. Quantum Hydrogen-Bond Symmetrization in the Superconducting Hydrogen Sulfide System. *Nature* **2016**, *532*, 81–84. [CrossRef] [PubMed]
79. Lyakhov, A.O.; Oganov, A.R.; Stokes, H.T.; Zhu, Q. New Developments in Evolutionary Structure Prediction Algorithm USPEX. *Comput. Phys. Commun.* **2013**, *184*, 1172–1182. [CrossRef]
80. Goncharenko, I.; Eremets, M.I.; Hanfland, M.; Tse, J.S.; Amboage, M.; Yao, Y.; Trojan, I.A. Pressure-Induced Hydrogen-Dominant Metallic State in Aluminum Hydride. *Phys. Rev. Lett.* **2008**, *100*, 045504. [CrossRef] [PubMed]
81. Singh, D.; Cohen, R.E.; Papaconstantopoulos, D.A. Possiblity of LiPdHx as a New Ionic Superconductor. *Phys. Rev. B* **1990**, *41*, 861–864. [CrossRef]
82. Talantsev, E.F.; Tallon, J.L. Universal Self-Field Critical Current for Thin-Film Superconductors. *Nat. Commun.* **2015**, *6*, 7820. [CrossRef]
83. Talantsev, E.F.; Crump, W.P.; Tallon, J.L. Universal Scaling of the Self-Field Critical Current in Superconductors: From Sub-Nanometre to Millimetre Size. *Sci. Rep.* **2017**, *7*, 10010. [CrossRef]
84. Park, S.; Kim, S.Y.; Kim, H.K.; Kim, M.J.; Kim, T.; Kim, H.; Choi, G.S.; Won, C.J.; Kim, S.; Kim, K.; et al. Superconductivity Emerging from a Stripe Charge Order in $IrTe_2$ Nanoflakes. *Nat. Commun.* **2021**, *12*, 3157. [CrossRef] [PubMed]
85. Talantsev, E.F.; Crump, W.P.; Storey, J.G.; Tallon, J.L. London Penetration Depth and Thermal Fluctuations in the Sulphur Hydride 203 K Superconductor. *Ann. Phys.* **2017**, *529*, 1600390. [CrossRef]
86. Khasanov, R.; Guguchia, Z.; Maisuradze, A.; Andreica, D.; Elender, M.; Raselli, A.; Shermadini, Z.; Goko, T.; Knecht, F.; Morenzoni, E.; et al. High Pressure Research Using Muons at the Paul Scherrer Institute. *High Press. Res.* **2016**, *36*, 140–166. [CrossRef]
87. Talantsev, E.F. Classifying Superconductivity in Compressed H_3S. *Mod. Phys. Lett. B* **2019**, *33*, 1950195. [CrossRef]
88. Talantsev, E.F. Electron–Phonon Coupling Constant and BCS Ratios in LaH_{10-y} Doped with Magnetic Rare-Earth Element. *Supercond. Sci. Technol.* **2022**, *35*, 095008. [CrossRef]
89. Khasanov, R. Perspective on Muon-Spin Rotation/Relaxation under Hydrostatic Pressure. *J. Appl. Phys.* **2022**, *132*, 190903. [CrossRef]
90. Grinenko, V.; Das, D.; Gupta, R.; Zinkl, B.; Kikugawa, N.; Maeno, Y.; Hicks, C.W.; Klauss, H.-H.; Sigrist, M.; Khasanov, R. Unsplit Superconducting and Time Reversal Symmetry Breaking Transitions in Sr_2RuO_4 under Hydrostatic Pressure and Disorder. *Nat. Commun.* **2021**, *12*, 3920. [CrossRef]
91. Talantsev, E.F. D-Wave Superconducting Gap Symmetry as a Model for $Nb_{1-x}Mo_xB_2$ (x = 0.25; 1.0) and WB_2 Diborides. *Symmetry* **2023**, *15*, 812. [CrossRef]
92. Migdal, A.B. Interaction between Electrons and Lattice Vibrations in a Normal Metal. *Sov. Phys.–JETP* **1958**, *7*, 996.
93. Eliashberg, G.M. Interactions between Electrons and Lattice Vibrations in a Superconductor. *Sov. Phys.–JETP* **1960**, *11*, 696.
94. Gor'kov, L.P. Phonon Mechanism in the Most Dilute Superconductor n-Type $SrTiO_3$. *Proc. Natl. Acad. Sci. USA* **2016**, *113*, 4646–4651. [CrossRef] [PubMed]
95. Takada, Y. Plasmon Mechanism of Superconductivity in Two- and Three-Dimensional Electron Systems. *J. Phys. Soc. Jpn.* **1978**, *45*, 786–794. [CrossRef]
96. Lin, X.; Zhu, Z.; Fauqué, B.; Behnia, K. Fermi Surface of the Most Dilute Superconductor. *Phys. Rev. X* **2013**, *3*, 021002. [CrossRef]
97. Szczeşńiak, D.; Drzazga-Szczeşńiak, E.A. Non-Adiabatic Superconductivity in the Electron-Doped Graphene. *Europhys. Lett.* **2021**, *135*, 67002. [CrossRef]
98. Drzazga-Szczęśniak, E.A.; Szczęśniak, D.; Kaczmarek, A.Z.; Szczęśniak, R. Breakdown of Adiabatic Superconductivity in Ca-Doped h-BN Monolayer. *Condens. Matter* **2022**, *7*, 60. [CrossRef]
99. Szczęśniak, D.; Kaczmarek, A.Z.; Drzazga-Szczęśniak, E.A.; Szczęśniak, R. Phonon-Mediated Superconductivity in Bismuthates by Nonadiabatic Pairing. *Phys. Rev. B* **2021**, *104*, 094501. [CrossRef]
100. Szcześniak, D. Scalability of Non-Adiabatic Effects in Lithium-Decorated Graphene Superconductor. *Europhys. Lett.* **2023**, *142*, 36002. [CrossRef]
101. Talantsev, E.F. Quantifying Nonadiabaticity in Major Families of Superconductors. *Nanomaterials* **2022**, *13*, 71. [CrossRef]
102. Yoon, H.; Swartz, A.G.; Harvey, S.P.; Inoue, H.; Hikita, Y.; Yu, Y.; Chung, S.B.; Raghu, S.; Hwang, H.Y. Low-Density Superconductivity in $SrTiO_3$ Bounded by the Adiabatic Criterion. *arXiv* **2021**, arXiv:2106.10802. [CrossRef]
103. Pietronero, L.; Strässler, S.; Grimaldi, C. Nonadiabatic Superconductivity. I. Vertex Corrections for the Electron-Phonon Interactions. *Phys. Rev. B* **1995**, *52*, 10516–10529. [CrossRef]

104. Grimaldi, C.; Pietronero, L.; Strässler, S. Nonadiabatic Superconductivity. II. Generalized Eliashberg Equations beyond Migdal's Theorem. *Phys. Rev. B* **1995**, *52*, 10530–10546. [CrossRef] [PubMed]
105. Cappelluti, E.; Ciuchi, S.; Grimaldi, C.; Pietronero, L.; Strässler, S. High Tc Superconductivity in MgB_2. *Phys. Rev. Lett.* **2002**, *88*, 117003. [CrossRef] [PubMed]
106. Grimaldi, C.; Cappelluti, E.; Pietronero, L. Isotope Effect on m * in High-Tc Materials Due to the Breakdown of Migdal's Theorem. *Europhys. Lett.* **1998**, *42*, 667–672. [CrossRef]
107. Pietronero, L.; Boeri, L.; Cappelluti, E.; Ortenzi, L. Conventional/Unconventional Superconductivity in High-Pressure Hydrides and beyond: Insights from Theory and Perspectives. *Quantum Stud. Math. Found.* **2018**, *5*, 5–21. [CrossRef]
108. Eremets, M.I.; Shimizu, K.; Kobayashi, T.C.; Amaya, K. Metallic CsI at Pressures of up to 220 Gigapascals. *Science* **1998**, *281*, 1333–1335. [CrossRef]
109. Talantsev, E.F. Fermi-Liquid Nonadiabatic Highly Compressed Cesium Iodide Superconductor. *Condens. Matter* **2022**, *7*, 65. [CrossRef]
110. Song, Y.; Bi, J.; Nakamoto, Y.; Shimizu, K.; Liu, H.; Zou, B.; Liu, G.; Wang, H.; Ma, Y. Stoichiometric Ternary Superhydride LaBeH8 as a New Template for High-Temperature Superconductivity at 110 K under 80 GPa. *Phys. Rev. Lett.* **2023**, *130*, 266001. [CrossRef]
111. Li, X.; Sun, J.; Shahi, P.; Gao, M.; MacDonald, A.H.; Uwatoko, Y.; Xiang, T.; Goodenough, J.B.; Cheng, J.; Zhou, J. Pressure-Induced Phase Transitions and Superconductivity in a Black Phosphorus Single Crystal. *Proc. Natl. Acad. Sci. USA* **2018**, *115*, 9935–9940. [CrossRef]
112. Guo, J.; Wang, H.; von Rohr, F.; Yi, W.; Zhou, Y.; Wang, Z.; Cai, S.; Zhang, S.; Li, X.; Li, Y.; et al. Electron-Hole Balance and the Anomalous Pressure-Dependent Superconductivity in Black Phosphorus. *Phys. Rev. B* **2017**, *96*, 224513. [CrossRef]
113. Shirotani, I.; Mikami, J.; Adachi, T.; Katayama, Y.; Tsuji, K.; Kawamura, H.; Shimomura, O.; Nakajima, T. Phase Transitions and Superconductivity of Black Phosphorus and Phosphorus-Arsenic Alloys at Low Temperatures and High Pressures. *Phys. Rev. B* **1994**, *50*, 16274–16278. [CrossRef]
114. Jin, M.; Wang, Q.; Liu, Y.; Zheng, Q.; Li, C.; Wang, S.; Wang, S.; Hao, N.; Nakamoto, Y.; Shimizu, K.; et al. Pressure Tuned 2D Superconductivity in Black Phosphorus. *arXiv* **2023**, arXiv:2307.08385. [CrossRef]
115. Bardeen, J.; Cooper, L.N.; Schrieffer, J.R. Theory of Superconductivity. *Phys. Rev.* **1957**, *108*, 1175–1204. [CrossRef]
116. McMillan, W.L. Transition Temperature of Strong-Coupled Superconductors. *Phys. Rev.* **1968**, *167*, 331–344. [CrossRef]
117. Dynes, R.C. McMillan's Equation and the Tc of Superconductors. *Solid State Commun.* **1972**, *10*, 615–618. [CrossRef]
118. Allen, P.B.; Dynes, R.C. Transition Temperature of Strong-Coupled Superconductors Reanalyzed. *Phys. Rev. B* **1975**, *12*, 905–922. [CrossRef]
119. Talantsev, E.F. Advanced McMillan's Equation and Its Application for the Analysis of Highly-Compressed Superconductors. *Supercond. Sci. Technol.* **2020**, *33*, 094009. [CrossRef]
120. Bloch, F. Zum Elektrischen Widerstandsgesetz Bei Tiefen Temperaturen. *Z. Für Phys.* **1930**, *59*, 208–214. [CrossRef]
121. Grüneisen, E. Die Abhängigkeit Des Elektrischen Widerstandes Reiner Metalle von Der Temperatur. *Ann. Phys.* **1933**, *408*, 530–540. [CrossRef]
122. Fisk, Z.; Webb, G.W. Saturation of the High-Temperature Normal-State Electrical Resistivity of Superconductors. *Phys. Rev. Lett.* **1976**, *36*, 1084–1086. [CrossRef]
123. Wiesmann, H.; Gurvitch, M.; Lutz, H.; Ghosh, A.; Schwarz, B.; Strongin, M.; Allen, P.B.; Halley, J.W. Simple Model for Characterizing the Electrical Resistivity in A−15 Superconductors. *Phys. Rev. Lett.* **1977**, *38*, 782–785. [CrossRef]
124. Carbotte, J.P. Properties of Boson-Exchange Superconductors. *Rev. Mod. Phys.* **1990**, *62*, 1027–1157. [CrossRef]
125. Helfand, E.; Werthamer, N.R. Temperature and Purity Dependence of the Superconducting Critical Field, Hc_2. II. *Phys. Rev.* **1966**, *147*, 288–294. [CrossRef]
126. Werthamer, N.R.; Helfand, E.; Hohenberg, P.C. Temperature and Purity Dependence of the Superconducting Critical Field, Hc_2. III. Electron Spin and Spin-Orbit Effects. *Phys. Rev.* **1966**, *147*, 295–302. [CrossRef]
127. Baumgartner, T.; Eisterer, M.; Weber, H.W.; Flükiger, R.; Scheuerlein, C.; Bottura, L. Effects of Neutron Irradiation on Pinning Force Scaling in State-of-the-Art Nb_3Sn Wires. *Supercond. Sci. Technol.* **2014**, *27*, 015005. [CrossRef]
128. Poole, C.P. Properties of the Normal Metallic State. In *Handbook of Superconductivity*; Elsevier: Amsterdam, The Netherlands, 2000; pp. 29–41.
129. Poole, C.P.; Farach, H.; Creswick, R.; Prozorov, R. *Superconductivity*, 2nd ed.; Academic Press: London, UK, 2007.
130. Talantsev, E.F. The Compliance of the Upper Critical Field in Magic-Angle Multilayer Graphene with the Pauli Limit. *Materials* **2022**, *16*, 256. [CrossRef]
131. Ho, C.Y.; Powell, R.W.; Liley, P.E. Thermal Conductivity of the Elements. *J. Phys. Chem. Ref. Data* **1972**, *1*, 279–421. [CrossRef]
132. Talantsev, E.F. The Dominance of Non-Electron–Phonon Charge Carrier Interaction in Highly-Compressed Superhydrides. *Supercond. Sci. Technol.* **2021**, *34*, 115001. [CrossRef]
133. Semenok, D. Computational Design of New Superconducting Materials and Their Targeted Experimental Synthesis. Ph.D. Thesis, Skolkovo Institute of Science and Technology, Moscow, Russia, 2022. [CrossRef]
134. Harshman, D.R.; Fiory, A.T. High-TC Superconductivity in Hydrogen Clathrates Mediated by Coulomb Interactions Between Hydrogen and Central-Atom Electrons. *J. Supercond. Nov. Magn.* **2020**, *33*, 2945–2961. [CrossRef]
135. Homes, C.C.; Dordevic, S.V.; Strongin, M.; Bonn, D.A.; Liang, R.; Hardy, W.N.; Komiya, S.; Ando, Y.; Yu, G.; Kaneko, N.; et al. A Universal Scaling Relation in High-Temperature Superconductors. *Nature* **2004**, *430*, 539–541. [CrossRef]

136. Koblischka, M.R.; Koblischka-Veneva, A. Calculation of Tc of Superconducting Elements with the Roeser–Huber Formalism. *Metals* **2022**, *12*, 337. [CrossRef]
137. Dew-Hughes, D. Flux Pinning Mechanisms in Type II Superconductors. *Philos. Mag.* **1974**, *30*, 293–305. [CrossRef]
138. Kramer, E.J. Scaling Laws for Flux Pinning in Hard Superconductors. *J. Appl. Phys.* **1973**, *44*, 1360–1370. [CrossRef]
139. Talantsev, E.F. New Scaling Laws for Pinning Force Density in Superconductors. *Condens. Matter* **2022**, *7*, 74. [CrossRef]
140. Godeke, A.; Haken, B.; Kate, H.H.J.; Larbalestier, D.C. A General Scaling Relation for the Critical Current Density in Nb_3Sn. *Supercond. Sci. Technol.* **2006**, *19*, R100–R116. [CrossRef]
141. Talantsev, E.F.; Mataira, R.C.; Crump, W.P. Classifying Superconductivity in Moiré Graphene Superlattices. *Sci. Rep.* **2020**, *10*, 212. [CrossRef]
142. Talantsev, E.F. Classifying Hydrogen-Rich Superconductors. *Mater. Res. Express* **2019**, *6*, 106002. [CrossRef]
143. Zhang, Z.; Cui, T.; Hutcheon, M.J.; Shipley, A.M.; Song, H.; Du, M.; Kresin, V.Z.; Duan, D.; Pickard, C.J.; Yao, Y. Design Principles for High-Temperature Superconductors with a Hydrogen-Based Alloy Backbone at Moderate Pressure. *Phys. Rev. Lett.* **2022**, *128*, 047001. [CrossRef]
144. Hirsch, J.E.; Marsiglio, F. On Magnetic Field Screening and Expulsion in Hydride Superconductors. *J. Supercond. Nov. Magn.* **2023**, *36*, 1257–1261. [CrossRef]
145. Hirsch, J.E.; Marsiglio, F. Evidence Against Superconductivity in Flux Trapping Experiments on Hydrides Under High Pressure. *J. Supercond. Nov. Magn.* **2022**, *35*, 3141–3145. [CrossRef]
146. Hirsch, J.E. Enormous Variation in Homogeneity and Other Anomalous Features of Room Temperature Superconductor Samples: A Comment on Nature 615, 244 (2023). *J. Supercond. Nov. Magn.* **2023**, *36*, 1489–1494. [CrossRef]
147. Hirsch, J.E. Electrical Resistance of Hydrides Under High Pressure: Evidence of Superconductivity or Confirmation Bias? *J. Supercond. Nov. Magn.* **2023**, *36*, 1495–1501. [CrossRef]
148. Talantsev, E.F. Classifying Induced Superconductivity in Atomically Thin Dirac-Cone Materials. *Condens. Matter* **2019**, *4*, 83. [CrossRef]